Supplement of Atmos. Chem. Phys., 23, 7975–8000, 2023
https://doi.org/10.5194/acp-23-7975-2023-supplement

Atmospheric Chemistry and Physics
Open Access
EGU

Supplement of

Complex refractive index and single scattering albedo of Icelandic dust in the shortwave part of the spectrum

Clarissa Baldo et al.

Correspondence to: Clarissa Baldo (clarissa.baldo@lisa.ipsl.fr)

Table S1: Sampling sites

Dust Hotspot	Location	Sample Code	Latitude / Longitude	Collection date
Dyngjusandur	NE Iceland	D3	64°50'41.885"N / 16°59'40.78"W	2016
Hagavatn	Central W Iceland	H55	64°28'52.04"N / 20°27'18.81"W	2015
Landeyjasandur	S Iceland	Land1	63°34'13"N / 20°02'31"W	2015
Mælifellssandur	Central S Iceland	Mæli2	63°48'42.2"N / 19°07'02.5"W	2013
Myrdalssandur	S Iceland	MIR45	63°32'42.08"N / 18°42'14.14"W	2015

Table S2: Experiment-averaged single scattering albedo $SSA_{avg}(\lambda)$ ± estimated uncertainty at λ = 370, 470, 520, 590, 660, 880, 950 nm of Icelandic dust for the base simulation, Test 1 and Test 2. In Test 1, corrections and calculations were performed using the SMPS and GRIMM data plus 1 SD uncertainty. In Test 2, we used the SMPS and GRIMM data minus 1 SD uncertainty (see section 2.2.1 in the main text for details).

Info	Sample ID	$SSA_{avg}(\lambda)$						
		370 nm	470 nm	520 nm	590 nm	660 nm	880 nm	950 nm
Base simulation	D3	0.93 ± 0.02	0.95 ± 0.01	0.96 ± 0.01	0.96 ± 0.01	0.96 ± 0.02	0.96 ± 0.01	0.96 ± 0.02
Base simulation	H55	0.94 ± 0.06	0.96 ± 0.08	0.96 ± 0.08	0.96 ± 0.08	0.96 ± 0.08	0.96 ± 0.07	0.96 ± 0.07
Base simulation	Land1	0.91 ± 0.05	0.94 ± 0.03	0.95 ± 0.03	0.95 ± 0.03	0.96 ± 0.04	0.96 ± 0.04	0.96 ± 0.04
Base simulation	Maeli2	0.90 ± 0.03	0.93 ± 0.02	0.94 ± 0.02	0.95 ± 0.02	0.95 ± 0.01	0.96 ± 0.01	0.95 ± 0.02
Base simulation	MIR45	0.90 ± 0.04	0.92 ± 0.03	0.93 ± 0.02	0.94 ± 0.03	0.94 ± 0.03	0.94 ± 0.03	0.94 ± 0.03
Test 1	D3	0.93 ± 0.02	0.95 ± 0.01	0.96 ± 0.01	0.96 ± 0.01	0.96 ± 0.02	0.96 ± 0.01	0.96 ± 0.01
Test 1	H55	0.94 ± 0.05	0.96 ± 0.07	0.96 ± 0.07	0.96 ± 0.08	0.96 ± 0.08	0.96 ± 0.07	0.96 ± 0.07
Test 1	Land1	0.91 ± 0.05	0.94 ± 0.03	0.95 ± 0.03	0.95 ± 0.03	0.96 ± 0.04	0.96 ± 0.04	0.96 ± 0.04
Test 1	Maeli2	0.90 ± 0.03	0.93 ± 0.02	0.94 ± 0.02	0.95 ± 0.02	0.95 ± 0.01	0.96 ± 0.02	0.96 ± 0.02
Test 1	MIR45	0.90 ± 0.04	0.92 ± 0.02	0.93 ± 0.02	0.94 ± 0.03	0.94 ± 0.03	0.94 ± 0.03	0.94 ± 0.03
Test 2	D3	0.93 ± 0.01	0.95 ± 0.01	0.96 ± 0.01	0.96 ± 0.02	0.96 ± 0.02	0.96 ± 0.02	0.96 ± 0.02
Test 2	H55	0.94 ± 0.06	0.96 ± 0.08	0.96 ± 0.08	0.96 ± 0.08	0.96 ± 0.08	0.96 ± 0.08	0.96 ± 0.08
Test 2	Land1	0.91 ± 0.04	0.93 ± 0.02	0.95 ± 0.03	0.95 ± 0.03	0.96 ± 0.03	0.96 ± 0.04	0.96 ± 0.04
Test 2	Maeli2	0.90 ± 0.02	0.93 ± 0.01	0.94 ± 0.01	0.95 ± 0.01	0.95 ± 0.01	0.95 ± 0.01	0.95 ± 0.01
Test 2	MIR45	0.90 ± 0.05	0.92 ± 0.04	0.93 ± 0.03	0.94 ± 0.04	0.94 ± 0.04	0.94 ± 0.04	0.94 ± 0.04

Table S3: Experiment-averaged imaginary index $k_{avg}(\lambda)$ ± estimated uncertainty at λ = 370, 470, 520, 590, 660, 880, 950 nm of Icelandic dust for the base simulation, Test 1 and Test 2. In Test 1, corrections and calculations were performed using the SMPS and GRIMM data plus 1 SD uncertainty. In Test 2, we used the SMPS and GRIMM data minus 1 SD uncertainty (see section 2.2.1 in the main text for details).

Info	Sample ID	$k_{avg}(\lambda)$						
		370 nm	470 nm	520 nm	590 nm	660 nm	880 nm	950 nm
Base simulation	D3	0.006 ± 0.003	0.005 ± 0.002	0.003 ± 0.002	0.002 ± 0.001	0.002 ± 0	0.002 ± 0	0.002 ± 0
Base simulation	H55	0.005 ± 0.002	0.005 ± 0.003	0.005 ± 0.002	0.002 ± 0.001	0.003 ± 0	0.002 ± 0	0.002 ± 0
Base simulation	Land1	0.005 ± 0.002	0.005 ± 0.003	0.005 ± 0.003	0.005 ± 0.002	0.004 ± 0.002	0.003 ± 0.001	0.002 ± 0.001
Base simulation	Maeli2	0.005 ± 0.003	0.005 ± 0.003	0.002 ± 0.002	0.004 ± 0.002	0.003 ± 0.001	0.002 ± 0.001	0.002 ± 0.001
Base simulation	MIR45	0.005 ± 0.002	0.005 ± 0.002	0.004 ± 0.001	0.004 ± 0.001	0.003 ± 0.001	0.003 ± 0	0.003 ± 0
Test 1	D3	0.002 ± 0.001	0.001 ± 0	0.001 ± 0	0.001 ± 0	0.001 ± 0	0.001 ± 0	0.001 ± 0
Test 1	H55	0.003 ± 0.001	0.002 ± 0.001	0.001 ± 0	0.001 ± 0	0.001 ± 0	0.002 ± 0.001	0.002 ± 0
Test 1	Land1	0.003 ± 0.002	0.002 ± 0	0.002 ± 0	0.001 ± 0	0.001 ± 0	0.001 ± 0.001	0.002 ± 0
Test 1	Maeli2	0.002 ± 0.001	0.002 ± 0.001	0.002 ± 0	0.002 ± 0	0.002 ± 0	0.002 ± 0	0.002 ± 0
Test 1	MIR45	0.002 ± 0.001	0.002 ± 0.001	0.002 ± 0.001	0.002 ± 0.001	0.002 ± 0.001	0.002 ± 0	0.002 ± 0
Test 2	D3	0.003 ± 0.001	0.002 ± 0	0.002 ± 0	0.002 ± 0	0.004 ± 0.002	0.002 ± 0	0.007 ± 0.002
Test 2	H55	0.002 ± 0	0.004 ± 0.001	0.005 ± 0.001	0.006 ± 0.002	0.007 ± 0	0.006 ± 0.002	0.007 ± 0
Test 2	Land1	0.005 ± 0	0.003 ± 0.001	0.003 ± 0.001	0.003 ± 0.001	0.004 ± 0.002	0.005 ± 0.001	0.006 ± 0.002
Test 2	Maeli2	0.004 ± 0	0.004 ± 0.002	0.002 ± 0.001	0.002 ± 0	0.002 ± 0	0.005 ± 0.001	0.005 ± 0.001
Test 2	MIR45	0.007 ± 0	0.006 ± 0	0.006 ± 0.001	0.005 ± 0	0.005 ± 0	0.006 ± 0	0.006 ± 0

Table S4: Experiment-averaged real index $n_{avg}(\lambda)$ ± estimated uncertainty at λ = 370, 470, 520, 590, 660, 880, 950 nm of Icelandic dust for the base simulation, Test 1 and Test 2. In Test 1, corrections and calculations were performed using the SMPS and GRIMM data plus 1 SD uncertainty. In Test 2, we used the SMPS and GRIMM data minus 1 SD uncertainty (see section 2.2.1 in the main text for details).

Info	Sample ID	$n_{avg}(\lambda)$						
		370 nm	470 nm	520 nm	590 nm	660 nm	880 nm	950 nm
Base simulation	D3	1.60 ± 0.02	1.61 ± 0.02	1.61 ± 0.02	1.61 ± 0.02	1.60 ± 0	1.60 ± 0	1.60 ± 0
Base simulation	H55	1.59 ± 0.02	1.60 ± 0.02	1.62 ± 0.01	1.61 ± 0.02	1.61 ± 0.03	1.60 ± 0	1.60 ± 0
Base simulation	Land1	1.59 ± 0.02	1.59 ± 0.01	1.60 ± 0.02	1.60 ± 0.02	1.61 ± 0.02	1.60 ± 0.02	1.61 ± 0.02
Base simulation	Maeli2	1.59 ± 0.02	1.60 ± 0.02	1.60 ± 0.03	1.61 ± 0.02	1.60 ± 0.02	1.61 ± 0.02	1.61 ± 0.02
Base simulation	MIR45	1.60 ± 0.02	1.60 ± 0.02	1.60 ± 0.02	1.59 ± 0.02	1.60 ± 0.02	1.60 ± 0.02	1.60 ± 0.02
Test 1	D3	1.60 ± 0.02	1.58 ± 0	1.58 ± 0	1.58 ± 0	1.60 ± 0.03	1.60 ± 0.03	1.60 ± 0.02
Test 1	H55	1.60 ± 0.02	1.60 ± 0.02	1.58 ± 0	1.59 ± 0.02	1.60 ± 0.02	1.59 ± 0.01	1.60 ± 0
Test 1	Land1	1.60 ± 0.02	1.60 ± 0	1.60 ± 0	1.60 ± 0.02	1.60 ± 0.02	1.60 ± 0.02	1.60 ± 0
Test 1	Maeli2	1.60 ± 0.02	1.60 ± 0.02	1.60 ± 0	1.60 ± 0	1.60 ± 0	1.60 ± 0	1.60 ± 0
Test 1	MIR45	1.60 ± 0.02	1.60 ± 0.02	1.60 ± 0.02	1.60 ± 0.02	1.61 ± 0.02	1.60 ± 0	1.60 ± 0
Test 2	D3	1.60 ± 0.02	1.60 ± 0.02	1.60 ± 0.02	1.59 ± 0.02	1.59 ± 0.02	1.58 ± 0	1.60 ± 0.02
Test 2	H55	1.60 ± 0.02	1.61 ± 0.02	1.62 ± 0.01	1.60 ± 0.02	1.59 ± 0	1.59 ± 0.02	1.63 ± 0
Test 2	Land1	1.62 ± 0.01	1.60 ± 0.02	1.60 ± 0.03	1.61 ± 0.03	1.60 ± 0.03	1.61 ± 0.02	1.60 ± 0.02
Test 2	Maeli2	1.62 ± 0.02	1.61 ± 0.02	1.60 ± 0.02	1.60 ± 0.02	1.60 ± 0.02	1.60 ± 0.02	1.61 ± 0.02
Test 2	MIR45	1.57 ± 0	1.59 ± 0.02	1.60 ± 0.02	1.62 ± 0	1.62 ± 0	1.58 ± 0.02	1.60 ± 0

Table S5: Comparison between $SSA_{avg}(\lambda)$ calculated using the measured Mie coefficients and the single scattering albedo retrieved using the complex refractive indices from the results of the base simulation, Test 1 and Test 2. In Test 1, corrections and calculations were performed using the SMPS and GRIMM data plus 1 SD uncertainty. In Test 2, we used the SMPS and GRIMM data minus 1 SD uncertainty (see section 2.2.1 in the main text for details). The reduced major axis (RMA) regression slope and intercept are reported, in addition to the R^2 value and root mean square error (RMSE).

Info	Sample ID	Slope	Intercept	R^2	RMSE
Base Simulation	D3	4.75	-3.62	0.84	0.06
Test 1	D3	1.15	-0.13	0.95	0.01
Test 2	D3	2.64	-1.59	0.29	0.04
Base Simulation	H55	6.69	-5.50	0.68	0.07
Test 1	H55	4.46	-3.33	0.95	0.03
Test 2	H55	-3.28	4.03	0.72	0.08
Base Simulation	Land1	2.72	-1.68	0.75	0.06
Test 1	Land1	1.92	-0.87	0.96	0.02
Test 2	Land1	1.62	-0.62	0.43	0.04
Base Simulation	Maeli2	2.49	-1.44	0.79	0.04
Test 1	Maeli2	0.76	0.22	0.88	0.01
Test 2	Maeli2	1.75	-0.72	0.59	0.03
Base Simulation	MIR45	2.46	-1.38	0.89	0.04
Test 1	MIR45	0.81	0.18	0.80	0.01
Test 2	MIR45	2.24	-1.20	0.95	0.05

Table S6: Reference complex refractive indices of the individual mineral components of Icelandic dust

Mineral	Reference	370 nm		470 nm		520 nm		590 nm		660 nm		880 nm		950 nm	
		n	k	n	k	n	k	n	k	n	k	n	k	n	k
Augite	Egan and Hilgeman (1979)	1.71	0.001	1.69	0.001	1.69	0.001	1.69	0.001	1.67	0.001	1.69	0.002	1.68	0.002
Basaltic glass	Pollack et al. (1973)	1.57	-	1.57	0.001	1.57	0.001	1.57	0	1.56	0	1.55	0.001	1.55	0.001
Feldspar	Egan and Hilgeman (1979)	1.59	0	1.57	0	1.58	0	1.57	0	1.56	0	1.56	0	1.56	0
Goethite	Bedidi and Cervelle (1993)	-	-	2.4	0.078	2.29	0.125	2.24	0.082	2.2	0.108	-	-	-	-
Hematite	(O-RAY) - Querry (1985)	2.47	1.202	3.24	0.874	3.26	0.587	3.31	0.202	3.05	0.051	2.81	0.026	2.79	0.022
Hematite	(E-RAY) - Querry (1985)	2.24	1.034	2.86	0.758	2.88	0.532	2.93	0.229	2.74	0.096	2.55	0.057	2.53	0.051
Hematite	Longtin et al. (1988)	2.56	0.793	2.99	0.274	3.1	0.149	3.06	0.053	2.97	0.006	2.73	0.004	2.71	0.002
Hematite	Bedidi and Cervelle (1993)	-	-	3.26	0.298	3.29	0.228	3.13	0.244	2.98	0.17	-	-	-	-
Hematite	Triaud (2005)	2.15	1.049	2.91	0.862	3.07	0.634	2.94	0.322	2.84	0.23	2.71	0.132	2.69	0.117
Magnetite	Querry (1985)	2.45	0.108	2.37	0.054	2.35	0.083	2.34	0.131	2.36	0.137	2.21	0.173	2.16	0.234
Magnetite	Huffman and Stapp (1973)	2.34	0.843	2.47	0.698	2.51	0.634	2.55	0.578	2.56	0.498	2.42	0.37	2.35	0.415
Olivine	Fabian et al. (2001)	-	-	1.85	0.001	1.85	0.001	1.85	0.001	1.85	0.001	1.85	0.001	1.85	0.002
Quartz	Gao et al. (2013)	1.49	0	1.48	0	1.48	0	1.48	0	1.48	0	1.47	0	1.47	0
Quartz	Rodríguez-de Marcos et al. (2016)	1.48	0.003	1.47	0.002	1.47	0.002	1.46	0.002	1.46	0.002	1.46	0.001	1.46	0.001
Quartz	Lemarchand (2013)	1.49	0	1.48	0	1.48	0	1.47	0	1.47	0	1.47	0	1.47	0
Quartz glass	Khashan and Nasif (2001)	1.51	0	1.53	0	1.51	0	1.51	0	1.51	0	1.56	0	1.55	0
Quartz glass	Philip (1985)	1.54	0.001	1.53	0.002	1.53	0.002	1.53	0.002	1.53	0.002	1.52	0.004	1.51	0.004

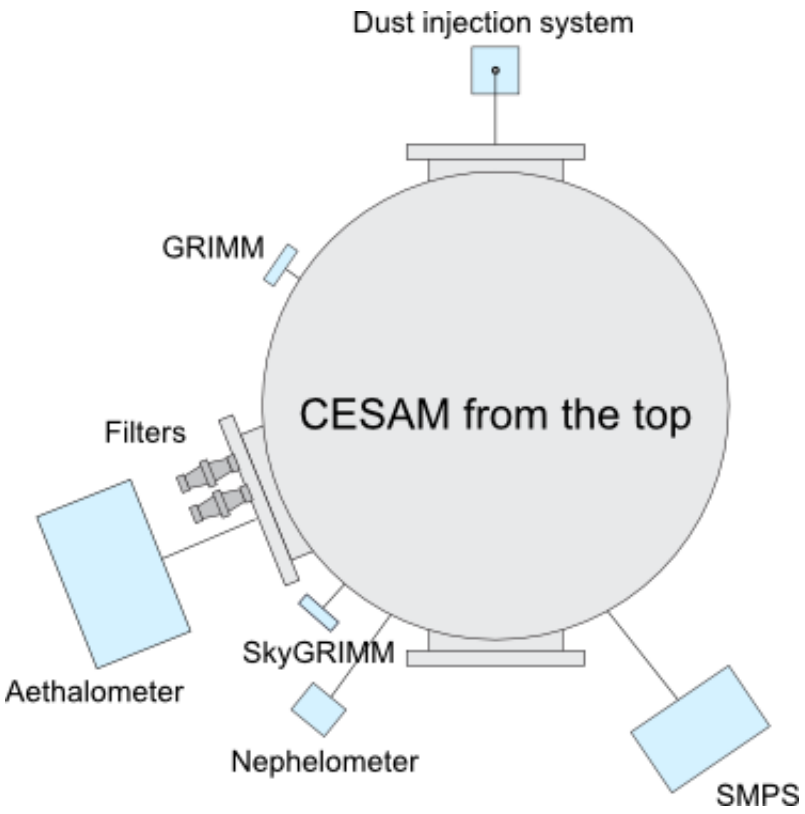

Figure S1: Schematic diagram of the CESAM set up for the experiments on Icelandic dust.

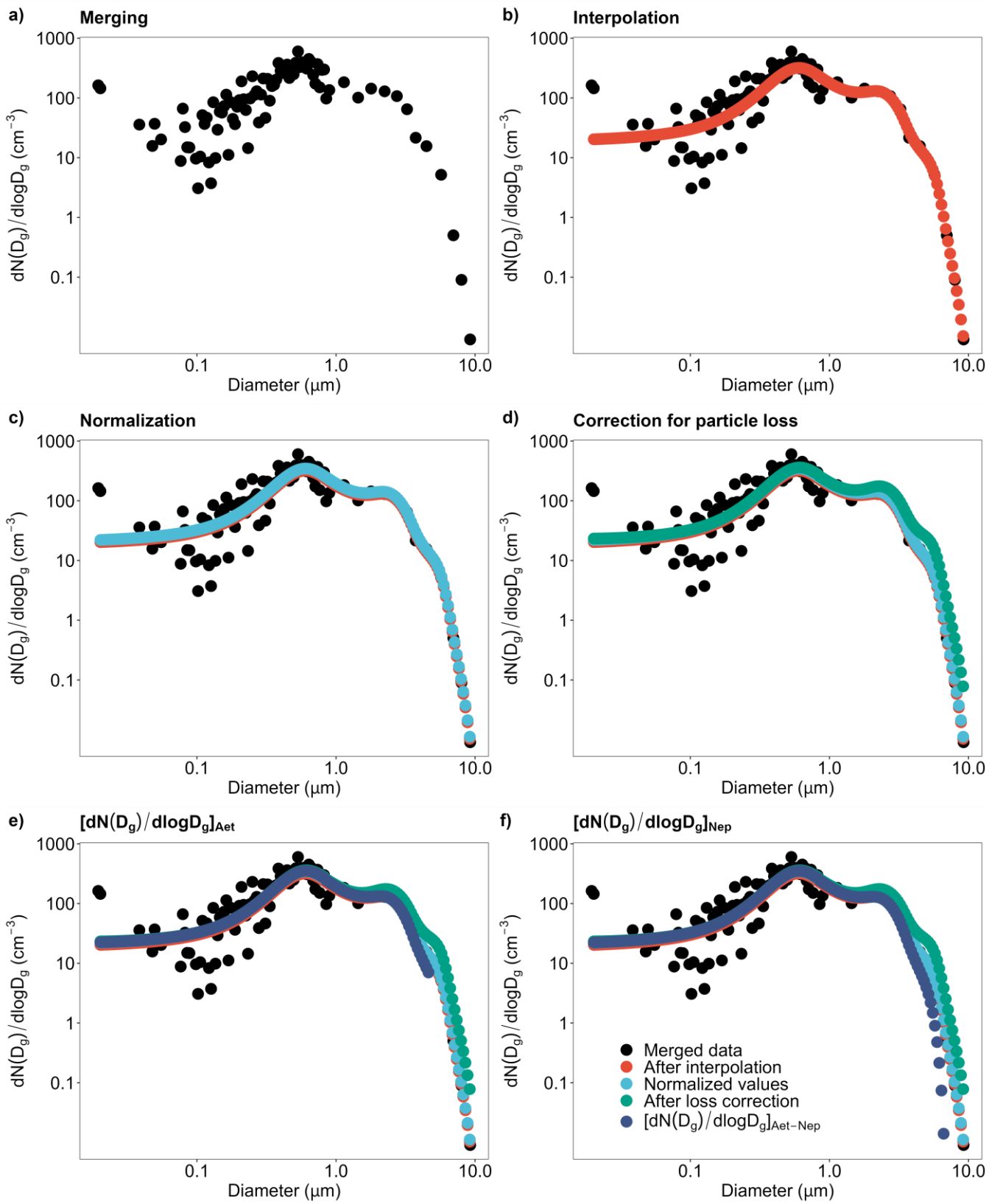

Figure S2: Processing of size distribution data. Geometrical size distributions $dN(D_g)/dlogD_g$ at 30 min after the injection peak obtained using the calibration values of the parameters χ, n, and k (χ = 1, n = 1.59, k = 0.000). a) Merging of the geometrical size distributions $dN/dlogD_g$ of SMPS and GRIMM; b) Interpolation of the merged size distribution; c) Normalization; d) Correction for particle loss to determine the real size distribution in CESAM. e-f) Size distribution of particles sampled by Shortwave Optical Properties Analyzers (SW-OPAs) Aethalometer (e) and nephelometer (f). Sample ID: Maeli2.

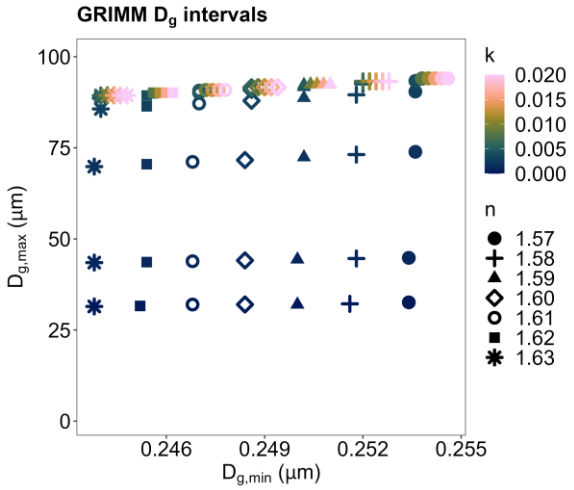

Figure S3: GRIMM D_g intervals. $D_{g,max}$ and $D_{g,min}$ are the upper and lower limit of the D_g intervals. n and k are respectively the real and imaginary part of the complex refractive indices used to convert the optical diameter D_{op} measured by the GRIMM into geometrical diameters D_g.

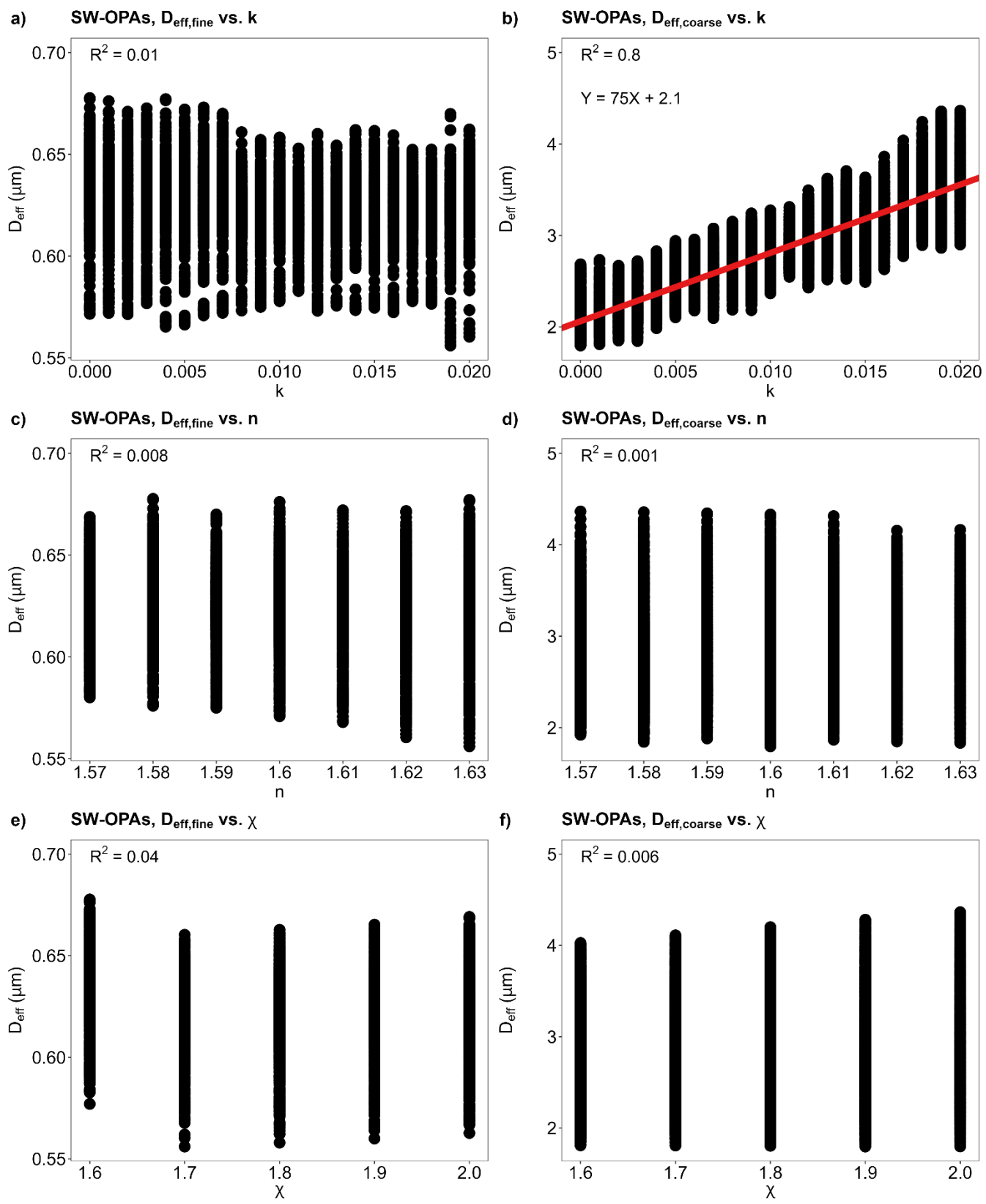

Figure S4: Comparison between the effective diameter of the coarse fractions ($D_{eff,coarse}$) and of the fine fractions ($D_{eff,fine}$) calculated using the SW-OPA size distributions and the input parameters χ, n, and k.

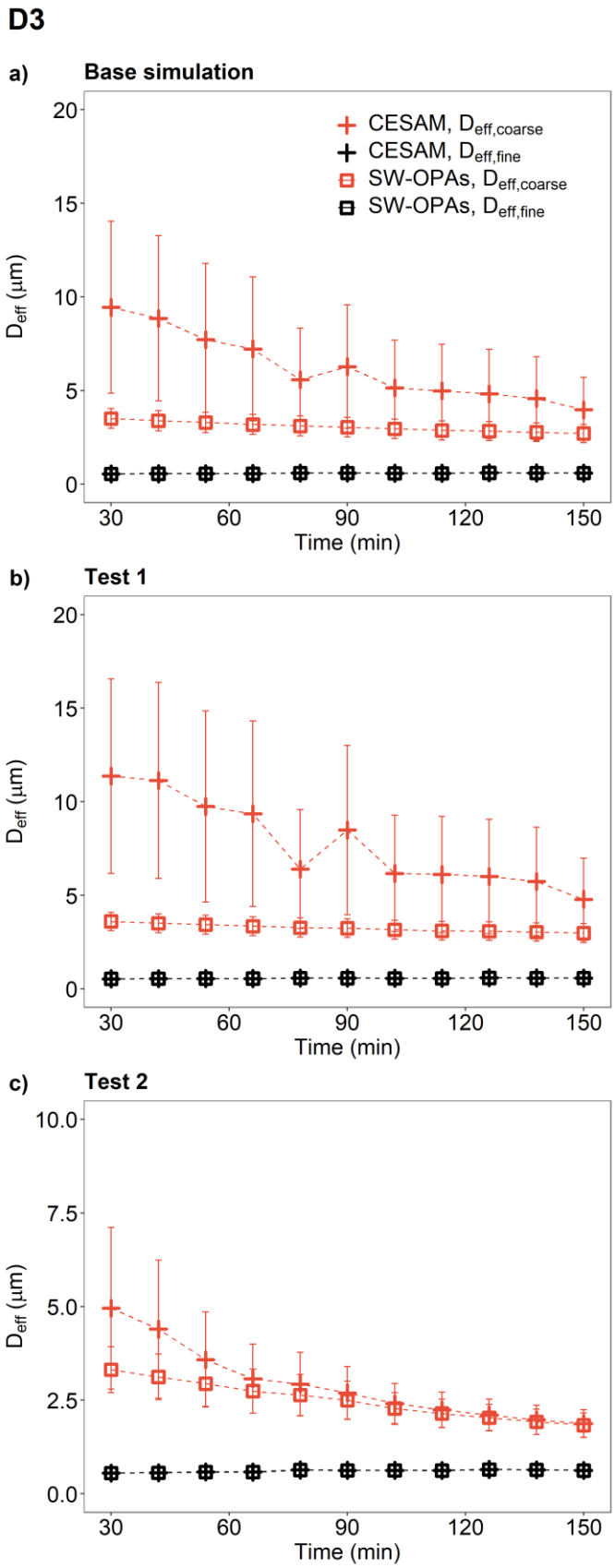

Figure S5: Effective diameters D_{eff} of dust particles sampled by the SW-OPAs and in CESAM, from 30 min after the injection peak to 2.5 h. a) Base simulation; b) Test 1; c) Test 2. D_{eff} was calculated for particles > 1 µm ($D_{eff,coarse}$) and ≤ 1 µm ($D_{eff,fine}$). Data were reported as 12-min average. In Test 1, corrections and calculations were performed using the SMPS and GRIMM data plus 1 SD uncertainty. In Test 2, we used the SMPS and GRIMM data minus 1 SD uncertainty (see section 2.2.1 in the main text for details). Sample ID: D3.

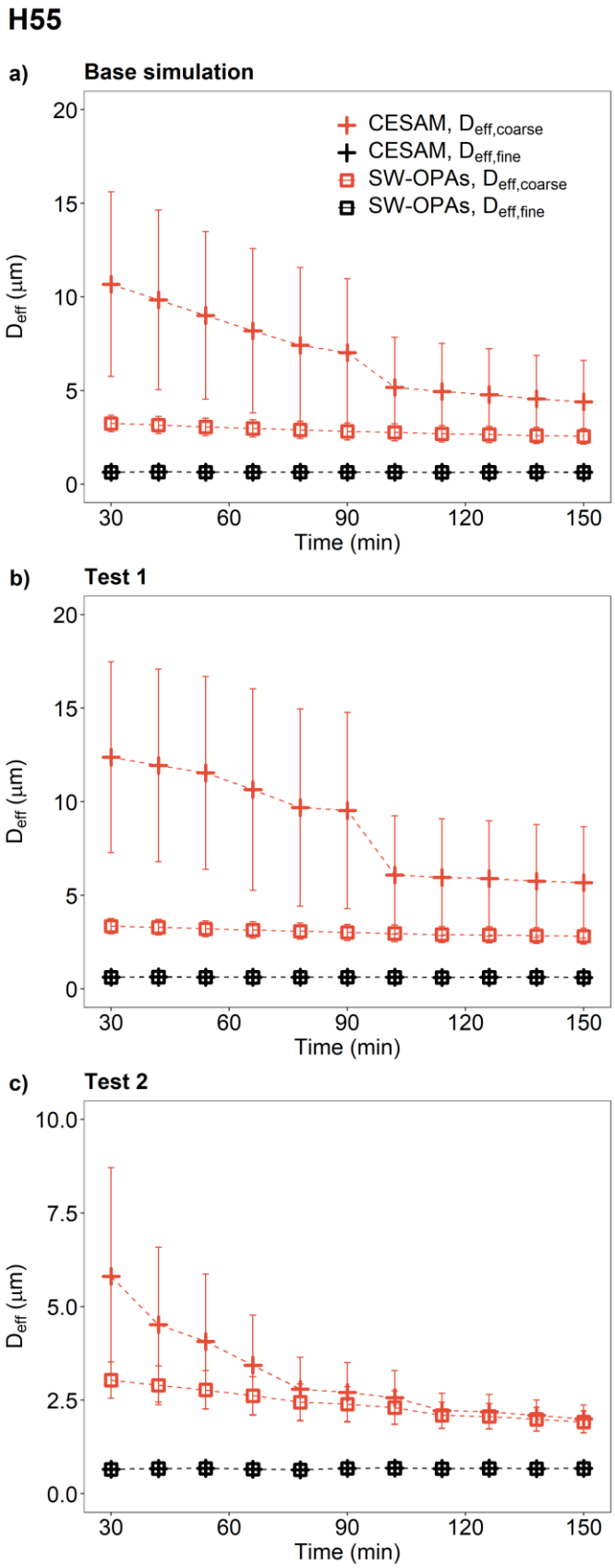

Figure S6: Effective diameters D_{eff} of dust particles sampled by the SW-OPAs and in CESAM, from 30 min after the injection peak to 2.5 h. a) Base simulation; b) Test 1; c) Test 2. D_{eff} was calculated for particles > 1 µm ($D_{eff,coarse}$) and ≤ 1 µm ($D_{eff,fine}$). Data were reported as 12-min average. In Test 1, corrections and calculations were performed using the SMPS and GRIMM data plus 1 SD uncertainty. In Test 2, we used the SMPS and GRIMM data minus 1 SD uncertainty (see section 2.2.1 in the main text for details). Sample ID: H55.

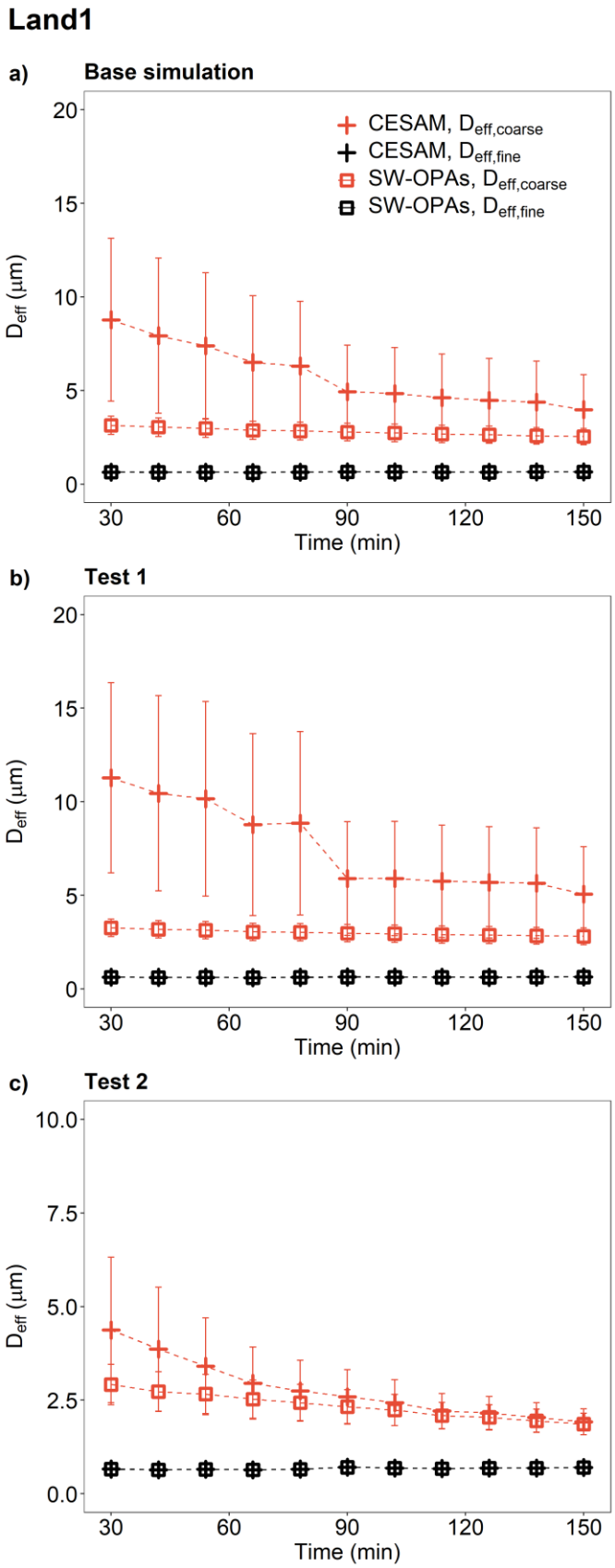

Figure S7: Effective diameters D_{eff} of dust particles sampled by the SW-OPAs and in CESAM, from 30 min after the injection peak to 2.5 h. a) Base simulation; b) Test 1; c) Test 2. D_{eff} was calculated for particles > 1 µm ($D_{eff,coarse}$) and ≤ 1 µm ($D_{eff,fine}$). Data were reported as 12-min average. In Test 1, corrections and calculations were performed using the SMPS and GRIMM data plus 1 SD uncertainty. In Test 2, we used the SMPS and GRIMM data minus 1 SD uncertainty (see section 2.2.1 in the main text for details). Sample ID: Land1.

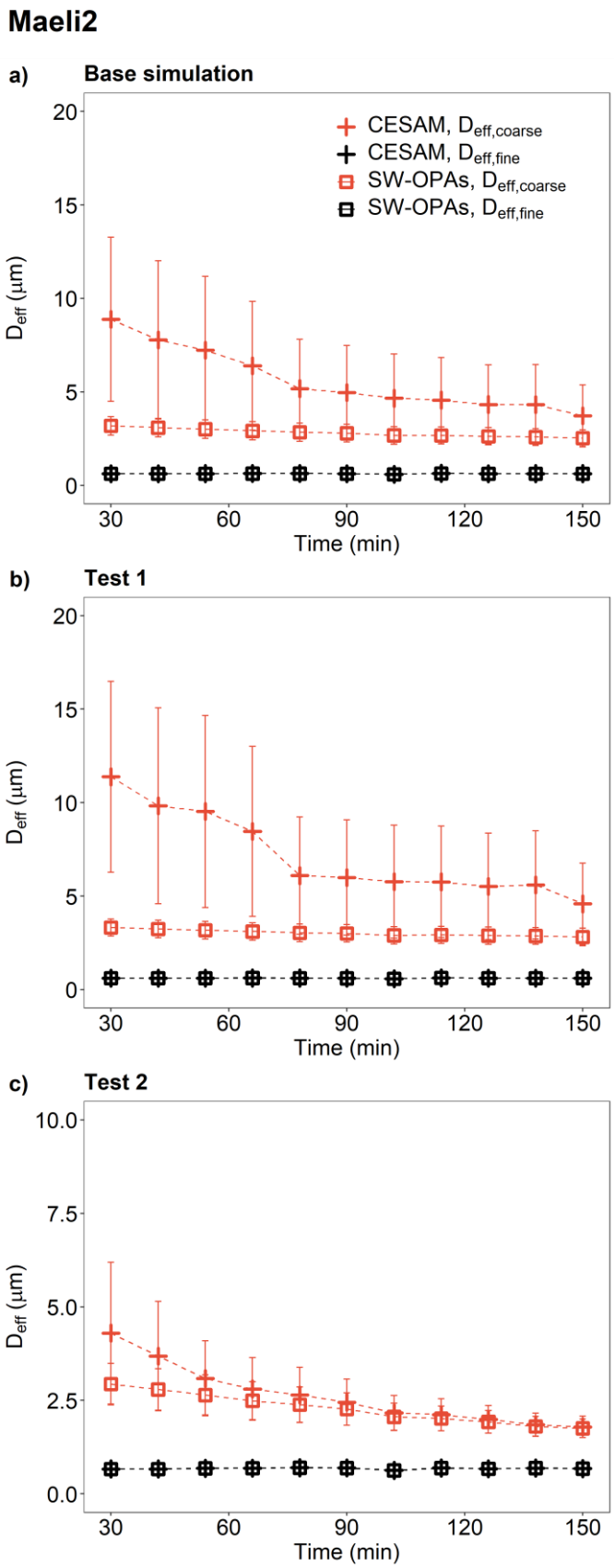

Figure S8: Effective diameters D_{eff} of dust particles sampled by the SW-OPAs and in CESAM, from 30 min after the injection peak to 2.5 h. a) Base simulation; b) Test 1; c) Test 2. D_{eff} was calculated for particles > 1 µm ($D_{eff,coarse}$) and ≤ 1 µm ($D_{eff,fine}$). Data were reported as 12-min average. In Test 1, corrections and calculations were performed using the SMPS and GRIMM data plus 1 SD uncertainty. In Test 2, we used the SMPS and GRIMM data minus 1 SD uncertainty (see section 2.2.1 in the main text for details). Sample ID: Maeli2.

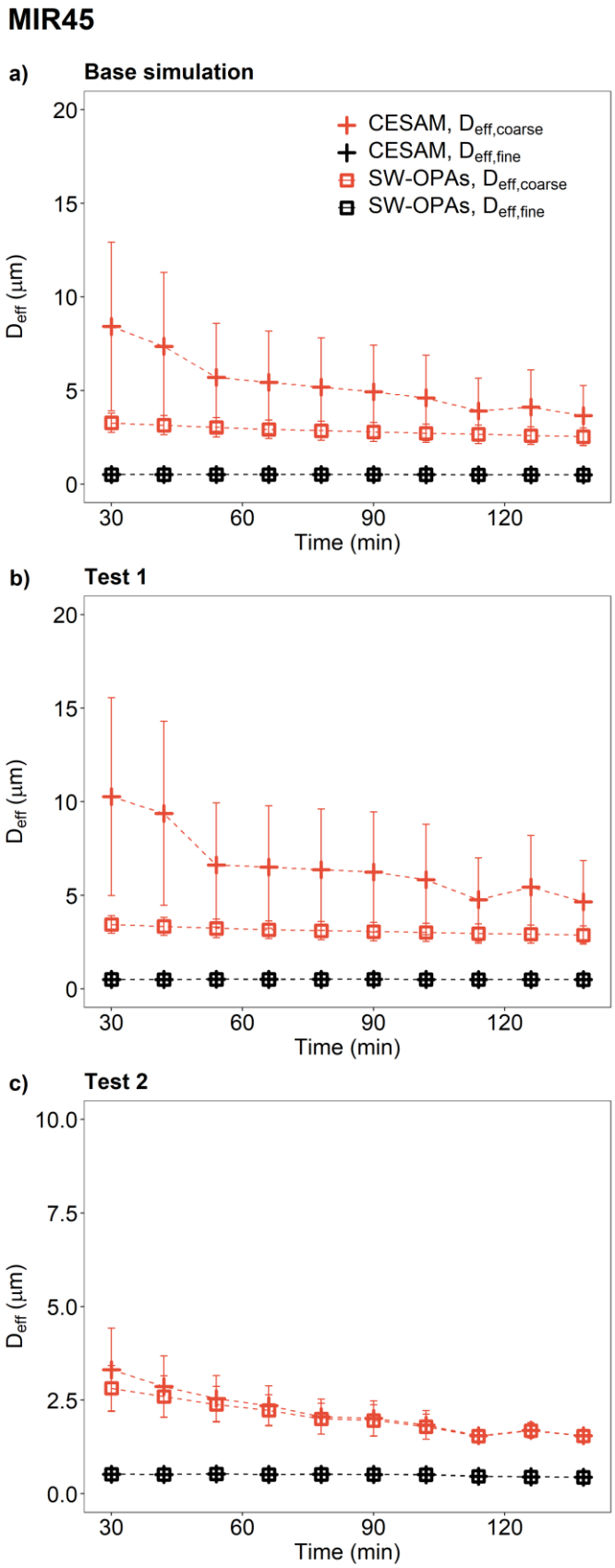

Figure S9: Effective diameters D_{eff} of dust particles sampled by the SW-OPAs and in CESAM, from 30 min after the injection peak to 2.5 h. a) Base simulation; b) Test 1; c) Test 2. D_{eff} was calculated for particles > 1 µm ($D_{eff,coarse}$) and ≤ 1 µm ($D_{eff,fine}$). Data were reported as 12-min average. In Test 1, corrections and calculations were performed using the SMPS and GRIMM data plus 1 SD uncertainty. In Test 2, we used the SMPS and GRIMM data minus 1 SD uncertainty (see section 2.2.1 in the main text for details). Sample ID: MIR45.

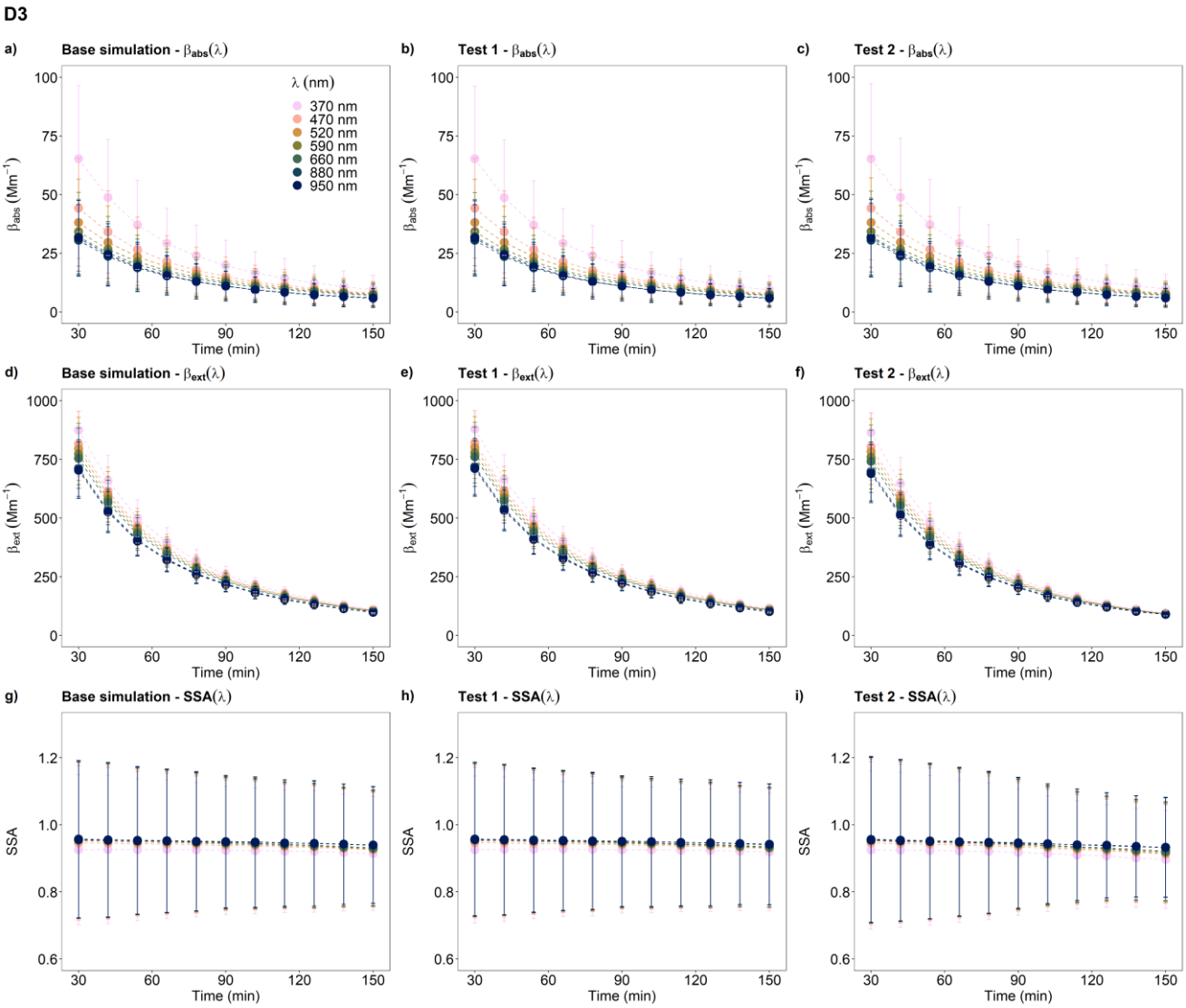

Figure S10: Extinction coefficient $\beta_{ext}(\lambda)$, absorption coefficient $\beta_{abs}(\lambda)$, and single scattering albedo SSA(λ) at λ = 370, 470, 520, 590, 660, 880, 950 nm, from 30 min after the injection peak to 2.5 h. a-c) Base simulation; d-f) Test 1; g-i) Test 2. Data were reported as 12-min average. In Test 1, corrections and calculations were performed using the SMPS and GRIMM data plus 1 SD uncertainty. In Test 2, we used the SMPS and GRIMM data minus 1 SD uncertainty (see section 2.2.1 in the main text for details). Sample ID: D3.

H55

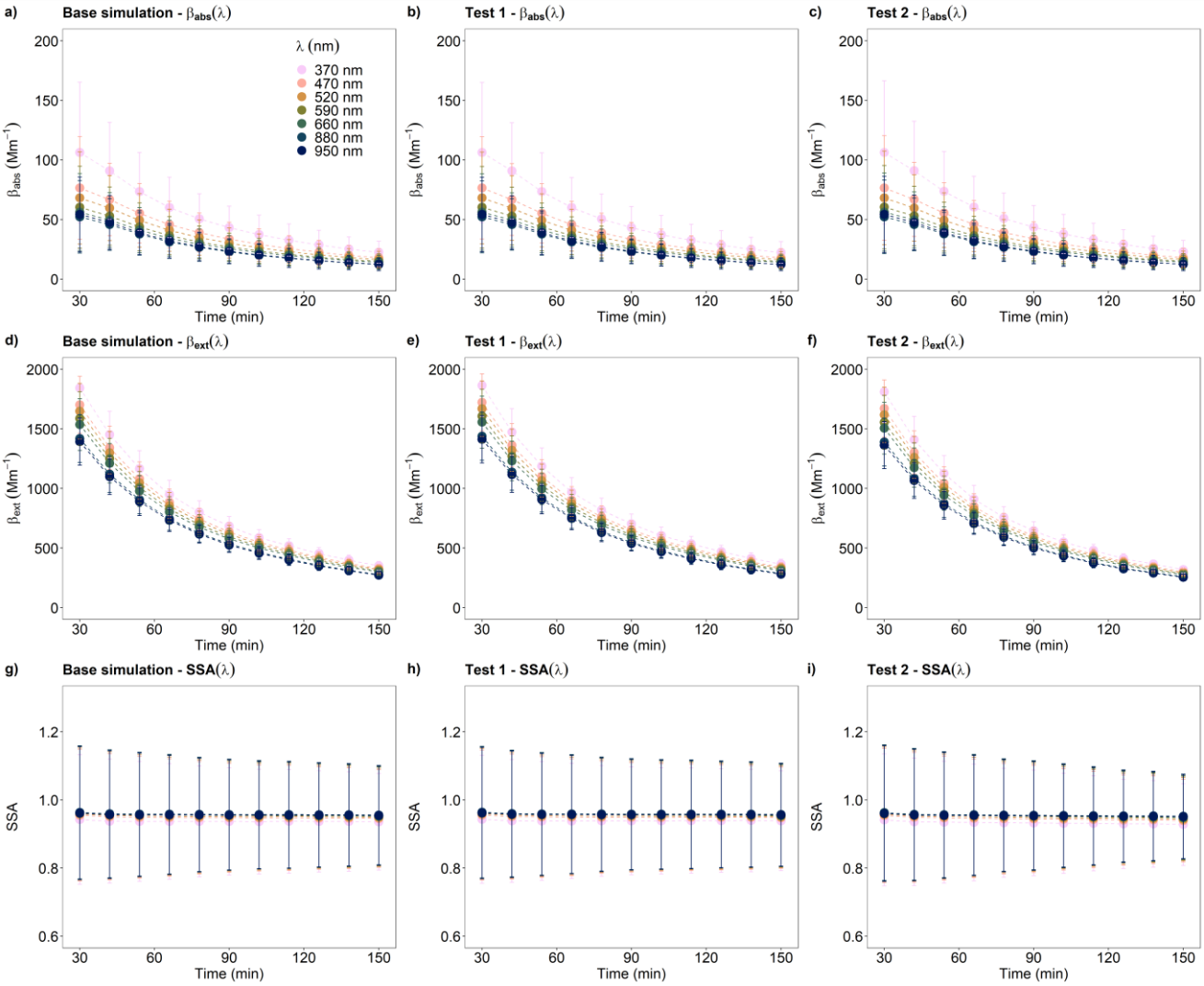

Figure S11: Extinction coefficient $\beta_{ext}(\lambda)$, absorption coefficient $\beta_{abs}(\lambda)$, and single scattering albedo SSA(λ) at λ = 370, 470, 520, 590, 660, 880, 950 nm, from 30 min after the injection peak to 2.5 h. a-c) Base simulation; d-f) Test 1; g-i) Test 2. Data were reported as 12-min average. In Test 1, corrections and calculations were performed using the SMPS and GRIMM data plus 1 SD uncertainty. In Test 2, we used the SMPS and GRIMM data minus 1 SD uncertainty (see section 2.2.1 in the main text for details). Sample ID: H55.

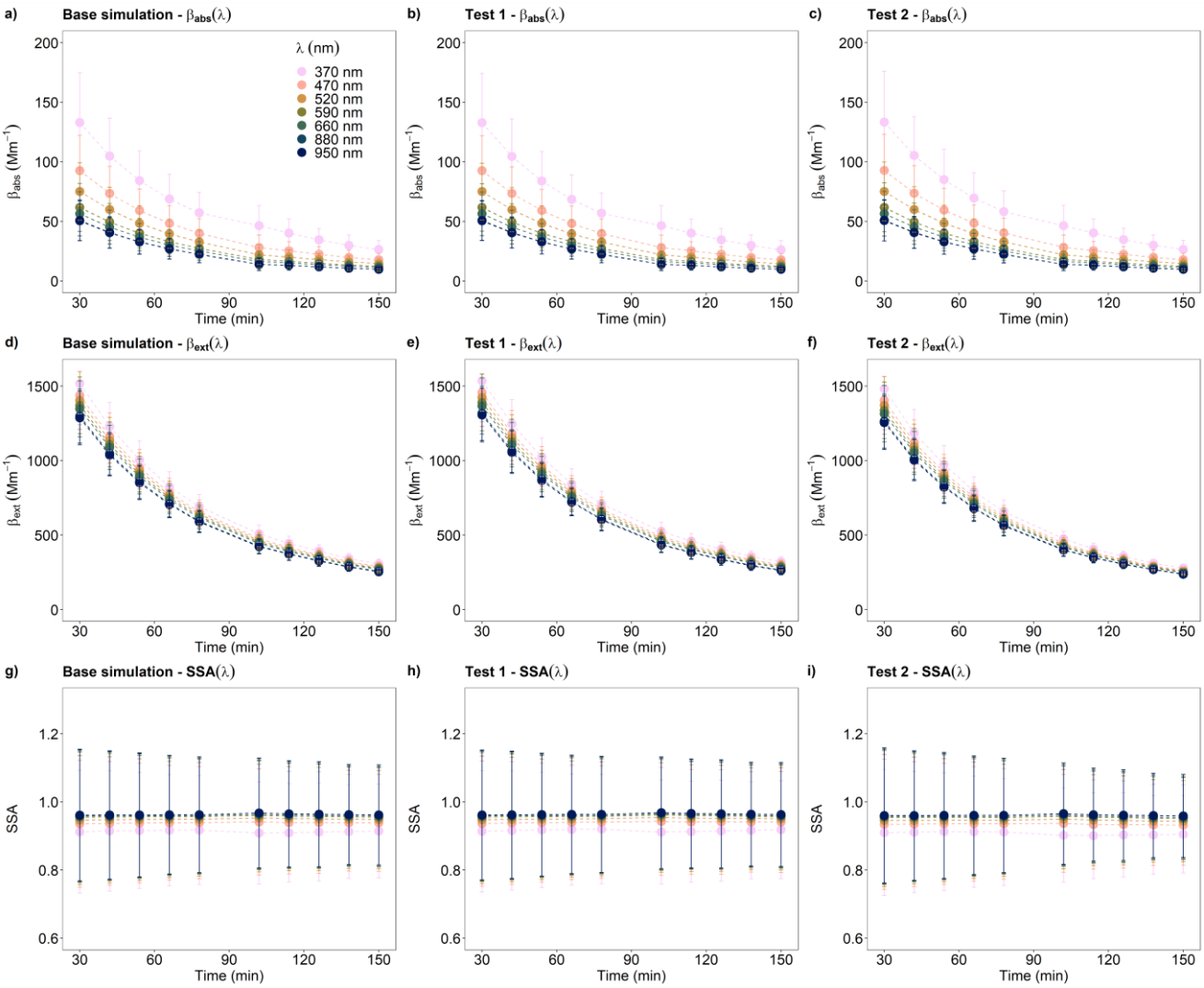

Figure S12: Extinction coefficient $\beta_{ext}(\lambda)$, absorption coefficient $\beta_{abs}(\lambda)$, and single scattering albedo SSA(λ) at λ = 370, 470, 520, 590, 660, 880, 950 nm, from 30 min after the injection peak to 2.5 h. a-c) Base simulation; d-f) Test 1; g-i) Test 2. Data were reported as 12-min average. In Test 1, corrections and calculations were performed using the SMPS and GRIMM data plus 1 SD uncertainty. In Test 2, we used the SMPS and GRIMM data minus 1 SD uncertainty (see section 2.2.1 in the main text for details). Sample ID: Land1.

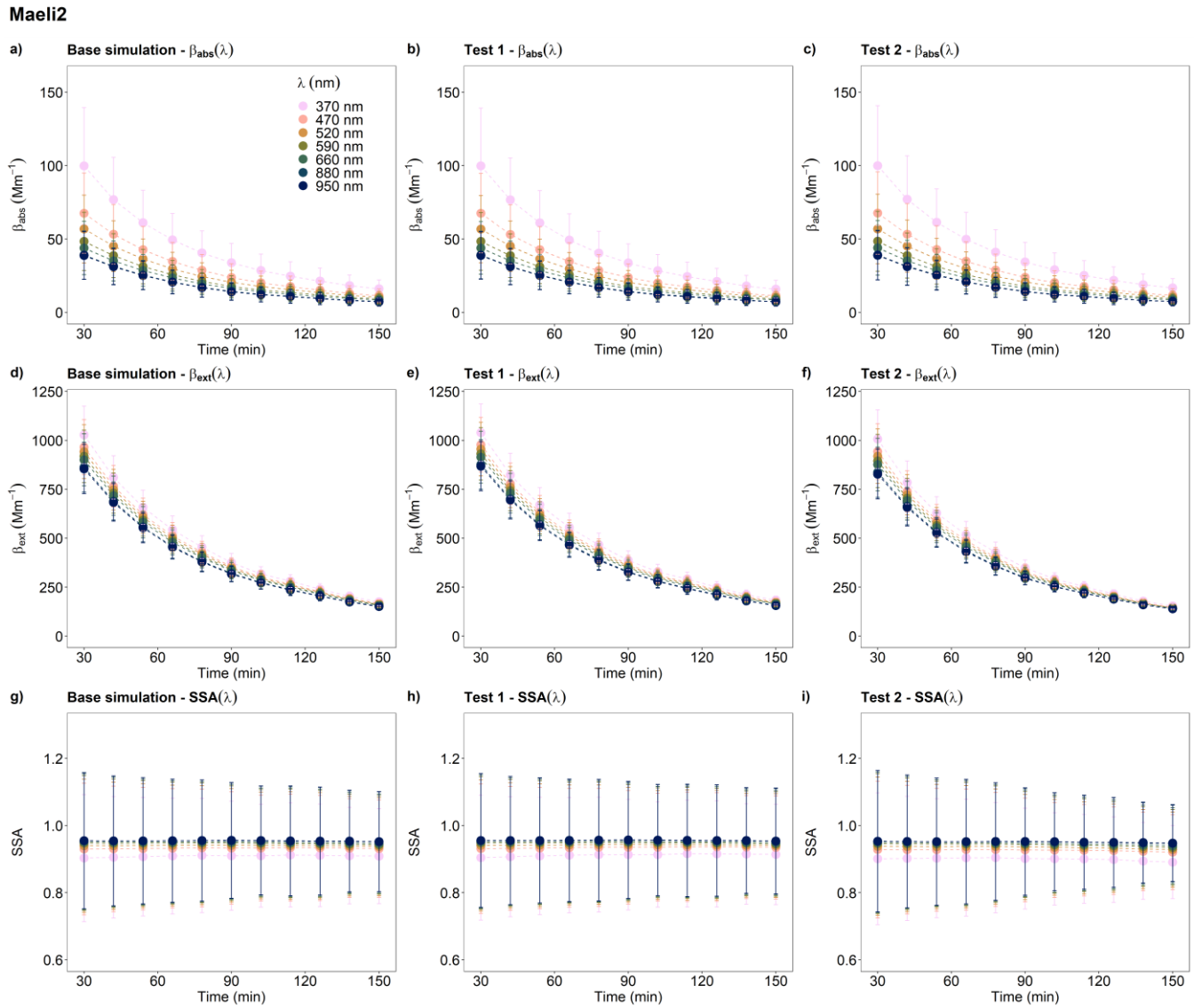

Figure S13: Extinction coefficient $\beta_{ext}(\lambda)$, absorption coefficient $\beta_{abs}(\lambda)$, and single scattering albedo SSA(λ) at λ = 370, 470, 520, 590, 660, 880, 950 nm, from 30 min after the injection peak to 2.5 h. a-c) Base simulation; d-f) Test 1; g-i) Test 2. Data were reported as 12-min average. In Test 1, corrections and calculations were performed using the SMPS and GRIMM data plus 1 SD uncertainty. In Test 2, we used the SMPS and GRIMM data minus 1 SD uncertainty (see section 2.2.1 in the main text for details). Sample ID: Maeli2.

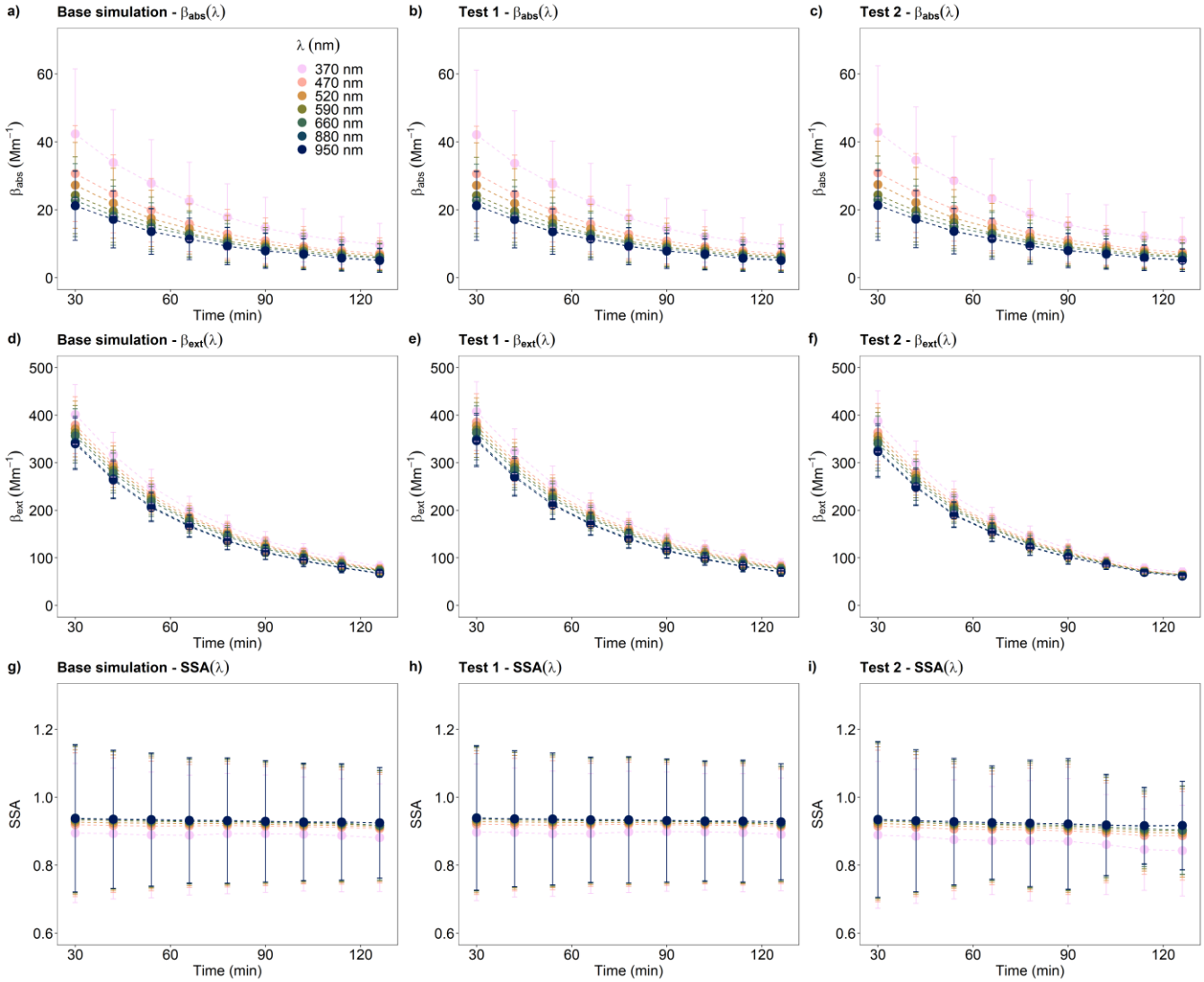

Figure S14: Extinction coefficient $\beta_{ext}(\lambda)$, absorption coefficient $\beta_{abs}(\lambda)$, and single scattering albedo SSA(λ) at λ = 370, 470, 520, 590, 660, 880, 950 nm, from 30 min after the injection peak to 2.5 h. a-c) Base simulation; d-f) Test 1; g-i) Test 2. Data were reported as 12-min average. In Test 1, corrections and calculations were performed using the SMPS and GRIMM data plus 1 SD uncertainty. In Test 2, we used the SMPS and GRIMM data minus 1 SD uncertainty (see section 2.2.1 in the main text for details). Sample ID: MIR45.

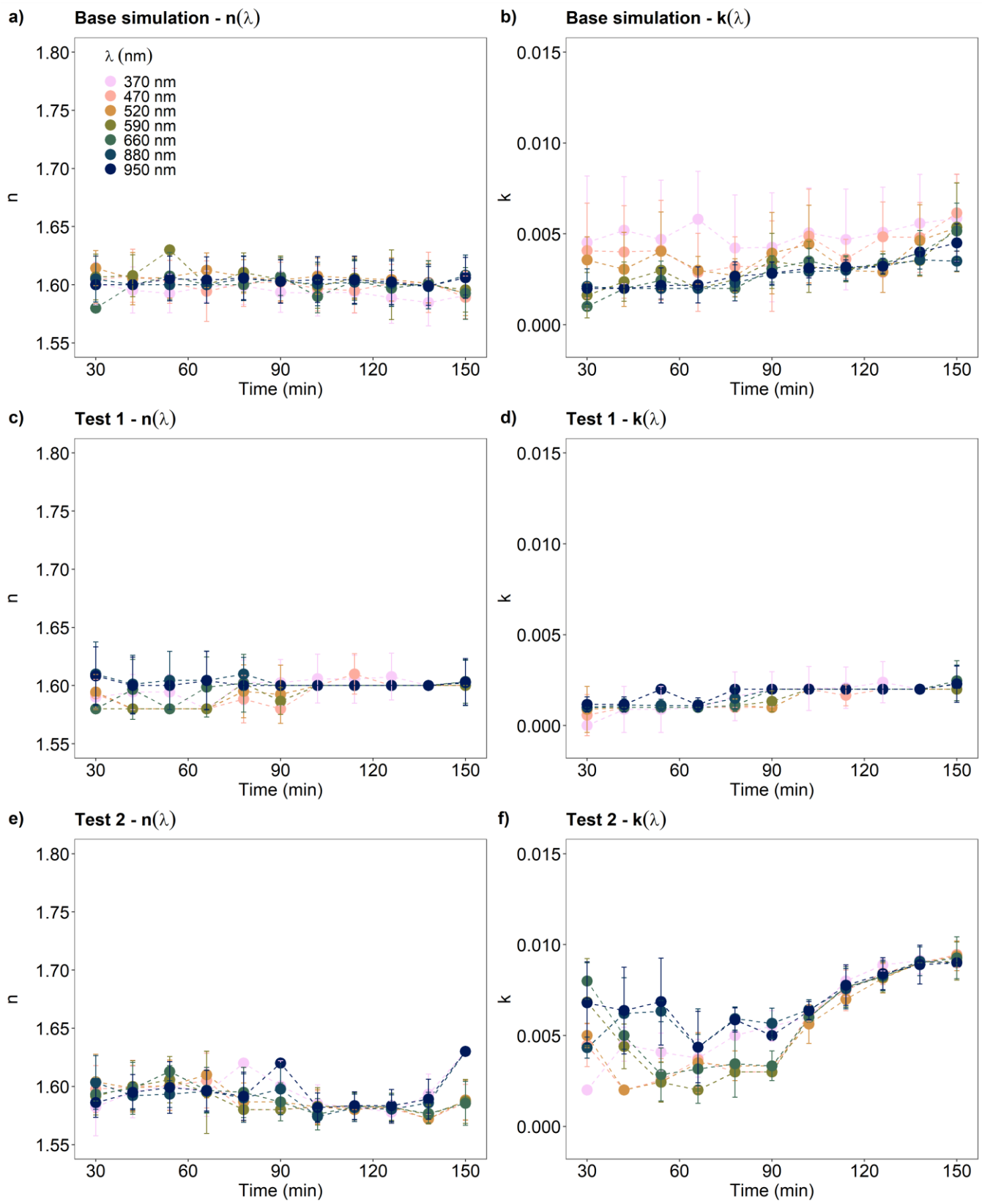

Figure S15: Real index n(λ) and imaginary index k(λ) at λ = 370, 470, 520, 590, 660, 880, 950 nm, from 30 min after the injection peak to 2.5 h. a-b) Base simulation; c-d) Test 1; e-f) Test 2. Data were retrieved at 12-min resolution. In Test 1, corrections and calculations were performed using the SMPS and GRIMM data plus 1 SD uncertainty. In Test 2, we used the SMPS and GRIMM data minus 1 SD uncertainty (see section 2.2.1 in the main text for details). Sample ID: D3.

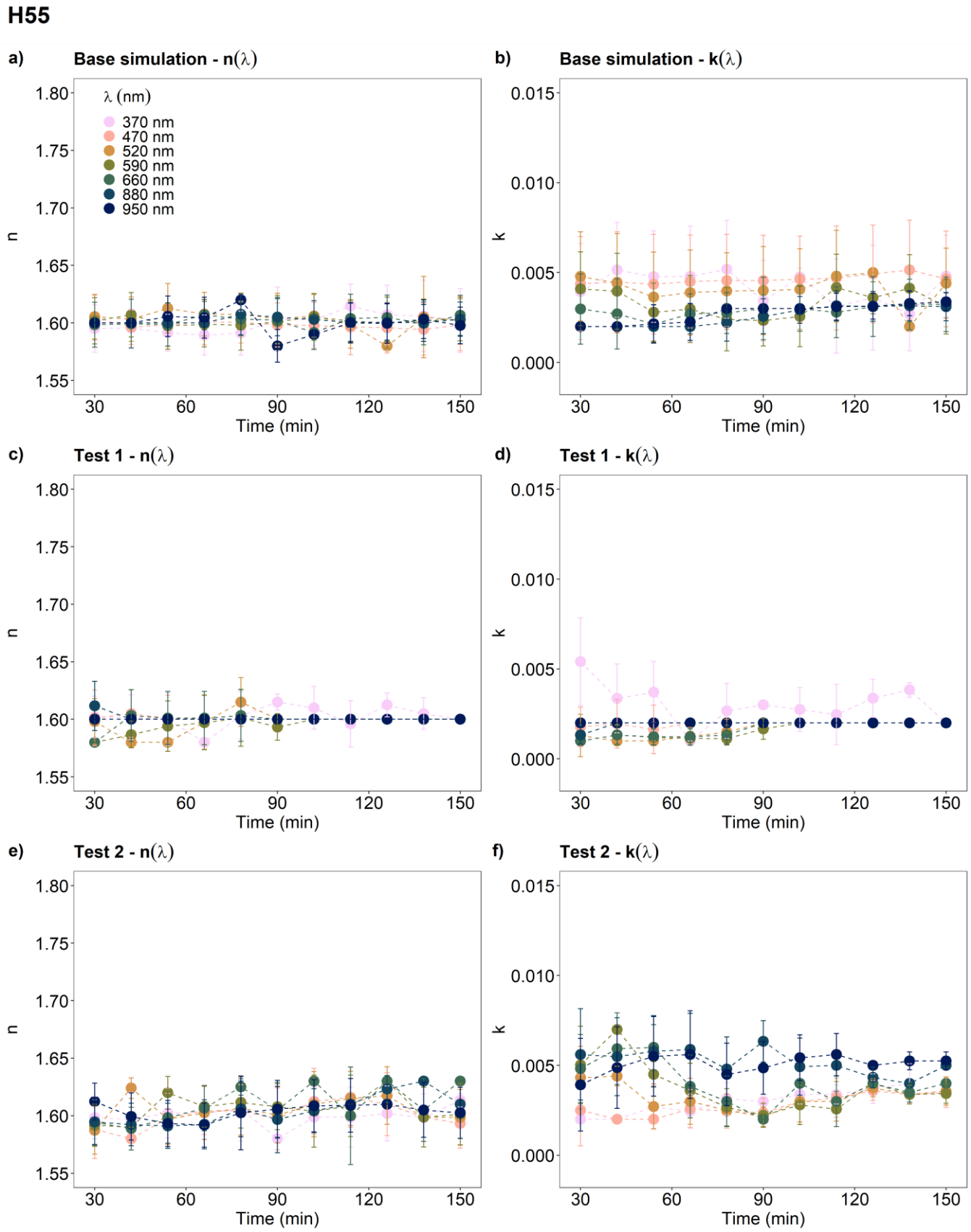

Figure S16: Real index n(λ) and imaginary index k(λ) at λ = 370, 470, 520, 590, 660, 880, 950 nm, from 30 min after the injection peak to 2.5 h. a-b) Base simulation; c-d) Test 1; e-f) Test 2. Data were retrieved at 12-min resolution. In Test 1, corrections and calculations were performed using the SMPS and GRIMM data plus 1 SD uncertainty. In Test 2, we used the SMPS and GRIMM data minus 1 SD uncertainty (see section 2.2.1 in the main text for details). Sample ID: H55.

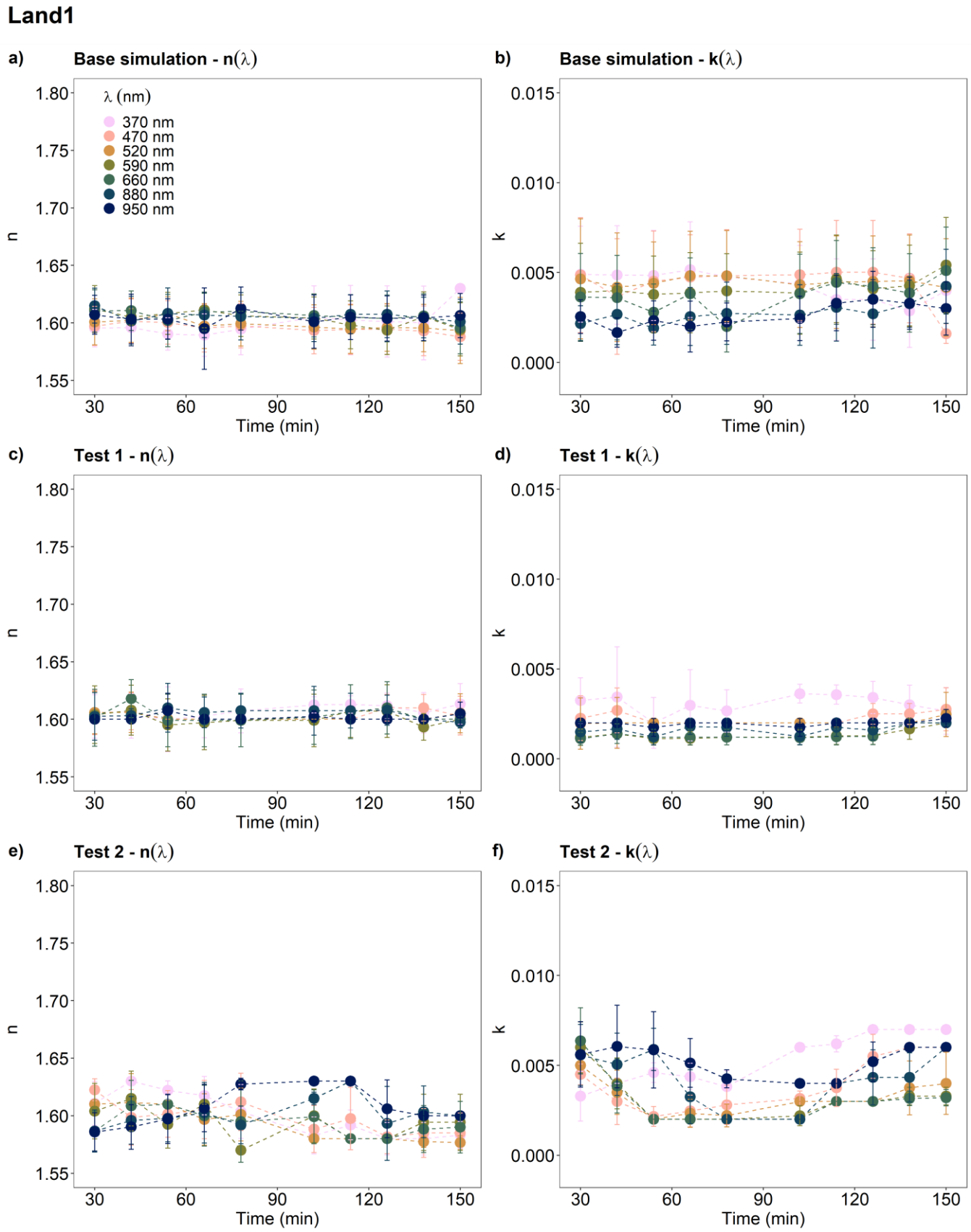

Figure S17: Real index n(λ) and imaginary index k(λ) at λ = 370, 470, 520, 590, 660, 880, 950 nm, from 30 min after the injection peak to 2.5 h. a-b) Base simulation; c-d) Test 1; e-f) Test 2. Data were retrieved at 12-min resolution. In Test 1, corrections and calculations were performed using the SMPS and GRIMM data plus 1 SD uncertainty. In Test 2, we used the SMPS and GRIMM data minus 1 SD uncertainty (see section 2.2.1 in the main text for details). Sample ID: Land1.

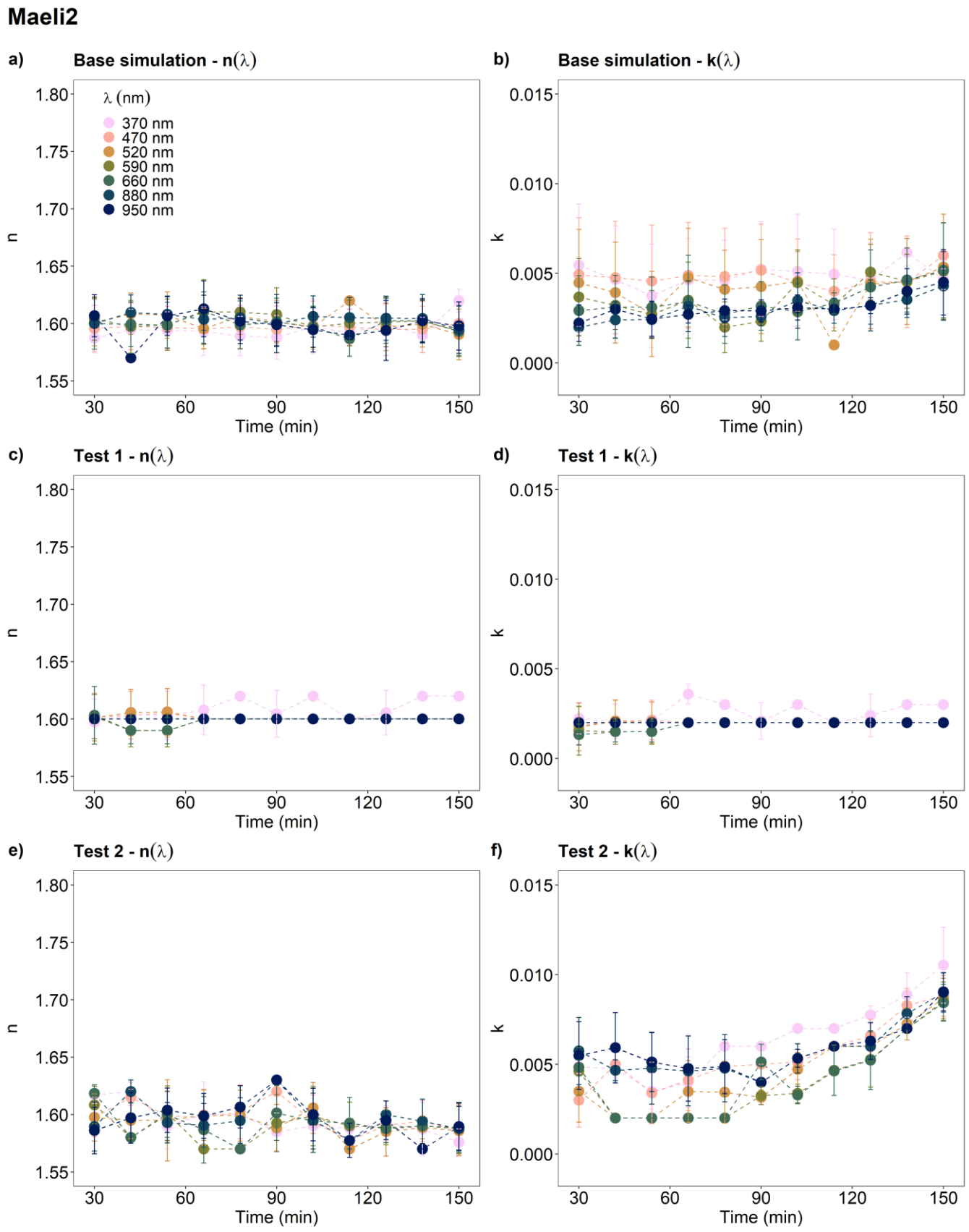

Figure S18: Real index n(λ) and imaginary index k(λ) at λ = 370, 470, 520, 590, 660, 880, 950 nm, from 30 min after the injection peak to 2.5 h. a-b) Base simulation; c-d) Test 1; e-f) Test 2. Data were retrieved at 12-min resolution. In Test 1, corrections and calculations were performed using the SMPS and GRIMM data plus 1 SD uncertainty. In Test 2, we used the SMPS and GRIMM data minus 1 SD uncertainty (see section 2.2.1 in the main text for details). Sample ID: Maeli2.

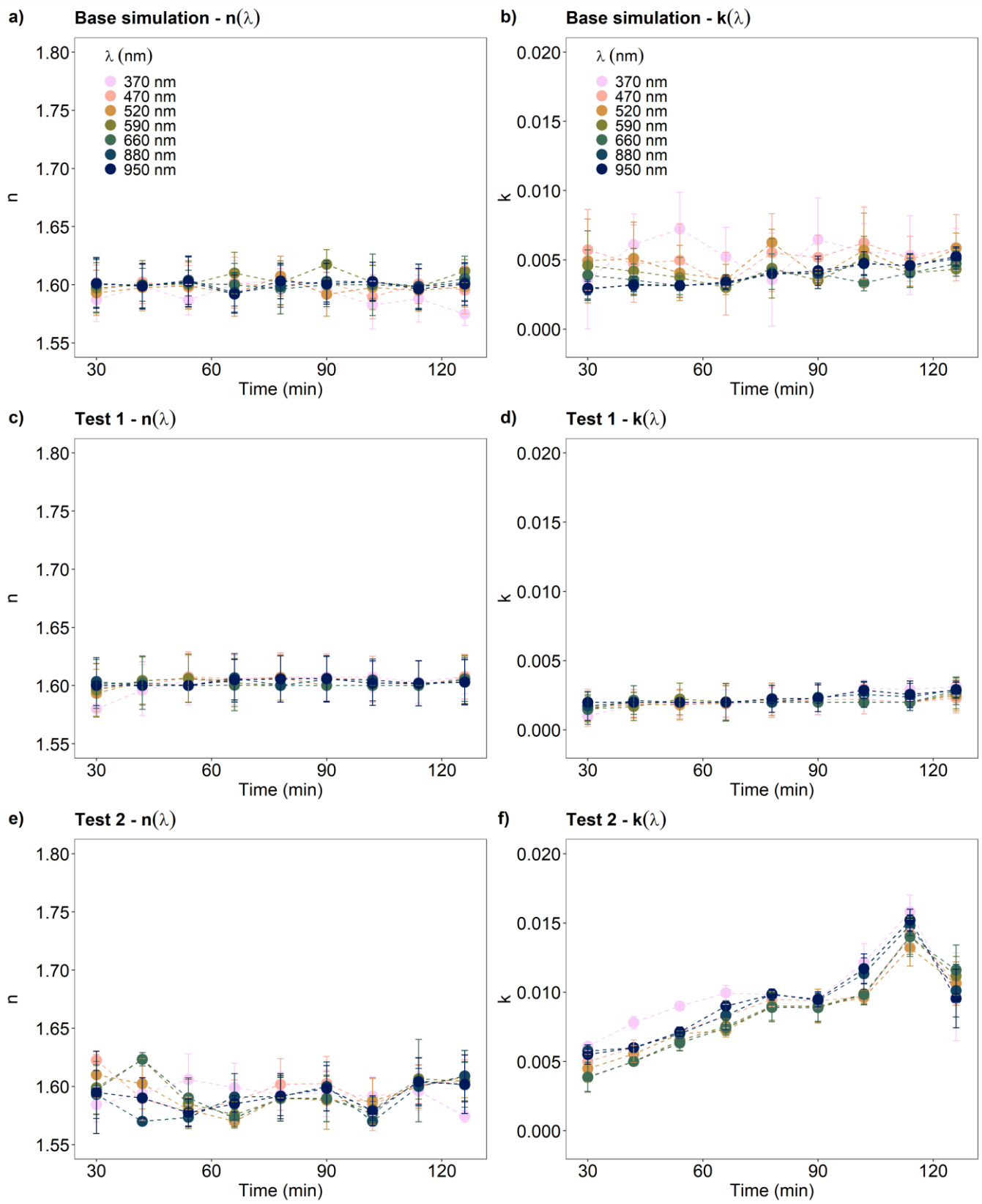

Figure S19: Real index n(λ) and imaginary index k(λ) at λ = 370, 470, 520, 590, 660, 880, 950 nm, from 30 min after the injection peak to 2.5 h. a-b) Base simulation; c-d) Test 1; e-f) Test 2. Data were retrieved at 12-min resolution. In Test 1, corrections and calculations were performed using the SMPS and GRIMM data plus 1 SD uncertainty. In Test 2, we used the SMPS and GRIMM data minus 1 SD uncertainty (see section 2.2.1 in the main text for details). Sample ID: MIR45.

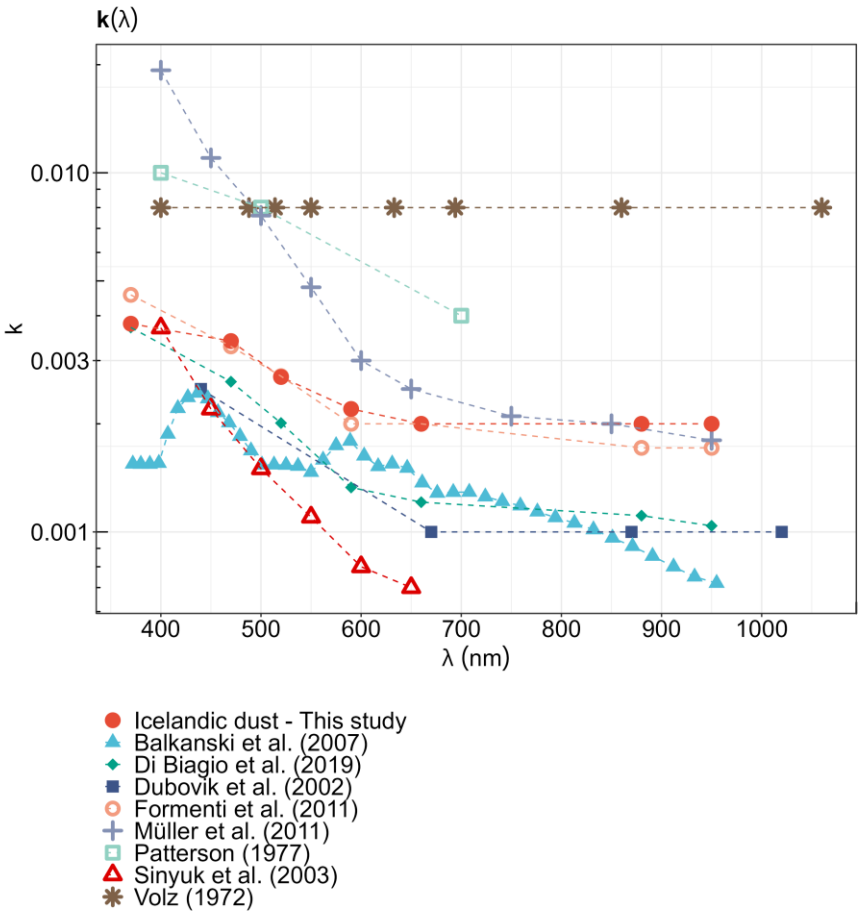

Figure S20: Comparison of the imaginary index k(λ) of Icelandic dust and that of mineral dust from low-latitude regions from the literature including: Di Biagio et al. (2019) (from laboratory experiments, here we report the average of k values obtained for northern African (Saharan) dust, Sahelian dust, and eastern Asian dust); Formenti et al. (2011) (from the AMMA campaign in Niger, here we report the average of airborne observations); Müller et al. (2011) (from the SAMUM campaign, measurements at Cape Verde Island during SAMUM-2); Balkanski et al. (2007) (calculated from mineralogy, here we report the k values obtained assuming a 1.5% hematite mass fraction in dust); Dubovik et al. (2002) (from AERONET measurements collected at the Bahrain–Persian Gulf and Solar Village–Saudi Arabia stations); Sinyuk et al. (2003) (from satellite observations of Saharan dust over Cape Verde, Dakar, and Burkina Faso); Volz (1972) (from laboratory experiments conducted on rainout dust collected in Germany); and Patterson et al. (1977) (from laboratory experiments conducted on Saharan dust).

References

Balkanski, Y., Schulz, M., Claquin, T., and Guibert, S.: Reevaluation of Mineral aerosol radiative forcings suggests a better agreement with satellite and AERONET data, Atmos. Chem. Phys., 7, 81-95, doi: 10.5194/acp-7-81-2007, 2007.

Bedidi, A., and Cervelle, B.: Light scattering by spherical particles with hematite and goethitelike optical properties: effect of water impregnation, Journal of Geophysical Research: Solid Earth, 98, 11941-11952, doi: 10.1029/93JB00188, 1993.

Di Biagio, C., Formenti, P., Balkanski, Y., Caponi, L., Cazaunau, M., Pangui, E., Journet, E., Nowak, S., Andreae, M. O., Kandler, K., Saeed, T., Piketh, S., Seibert, D., Williams, E., and Doussin, J. F.: Complex refractive indices and single-scattering albedo of global dust aerosols in the shortwave spectrum and relationship to size and iron content, Atmos. Chem. Phys., 19, 15503-15531, doi: 10.5194/acp-19-15503-2019, 2019.

Dubovik, O., Holben, B., Eck, T. F., Smirnov, A., Kaufman, Y. J., King, M. D., Tanre, D., and Slutsker, I.: Variability of absorption and optical properties of key aerosol types observed in worldwide locations, J. Atmos. Sci., 59, 590-608, doi: 10.1175/1520-0469(2002)059<0590:voaaop>2.0.co;2, 2002.

Egan, W., and Hilgeman, T.: Optical Properties of Inhomogeneous Materials: Applications to Geology, Astronomy, Chemistry and Engineering Academic Press, New York, 1979.

Fabian, D., Henning, Th., Joger, C., Mutschke, H., Dorschner, J., Werhan, O.: Olivine, EODG ARIA, available at http://eodg.atm.ox.ac.uk/ARIA/data?Minerals/Olivine/non-oriented_(Fabian_et_al._ 2001)/olivine_Fabian_2001.ri (last access: 02 January 2020), 2001.

Formenti, P., Rajot, J. L., Desboeufs, K., Said, F., Grand, N., Chevaillier, S., and Schmechtig, C.: Airborne observations of mineral dust over western Africa in the summer Monsoon season: spatial and vertical variability of physico-chemical and optical properties, Atmos. Chem. Phys., 11, 6387-6410, doi: 10.5194/acp-11-6387-2011, 2011.

Gao, L., Lemarchand, F., Lequime, M.: Quartz, Refractive index database, available at https://refractiveindex.info/ ?shelf=main&book=SiO2&page=Gao (last access: 05 January 2023), 2013.

Huffman, D. R., and Stapp, J. L.: Optical measurements on solids of possible interstellar importance, in: Interstellar dust and related topics, Springer, 297-301, 1973.

Khashan, M. A. and Nasif, A. Y.: Quartz glass, EODG ARIA, available at http://eodg.atm.ox.ac.uk/ARIA/data?Minerals/ Quartz/(Khashan_and Nassif_2001)/quartz_Khashan_2001.ri (last access: 02 January 2020), 2001.

Lemarchand, F.: Quartz, Refractive index database, available at https://refractiveindex.info/?shelf=main&book= SiO2&page=Lemarchand (last access: 05 January 2023), 2013.

Longtin, D. R., Shettle, E. P., Hummel, J. R., and Pryce, J. D.: A wind dependent desert aerosol model: Radiative properties, AFGLTR-88-0112, Air Force Geophysics Laboratory, Hanscom AFB, MA, 1988.

Müller, T., Schladitz, A., Kandler, K., and Wiedensohler, A.: Spectral particle absorption coefficients, single scattering albedos and imaginary parts of refractive indices from ground based in situ measurements at Cape Verde Island during SAMUM-2, Tellus Series B-Chemical and Physical Meteorology, 63, 573-588, doi: 10.1111/j.1600-0889.2011.00572.x, 2011.

Patterson, E. M., Gillette, D. A., and Stockton, B. H.: Complex index of refraction between 300 and 700 nm for Saharan aerosols, J. Geophys. Res., 82, 3153-3160, doi: 10.1029/JC082i021p03153, 1977.

Philip, H. R.: Quartz glass, EODG ARIA, available at http://eodg.atm.ox.ac.uk/ARIA/data?Minerals/Quartz/(Philipp_1985)/quartz_Philipp_1985.ri (last access: 05 January 2023), 1985.

Pollack, J. B., Toon, O. B., and Khare, B. N.: Optical properties of some terrestrial rocks and glasses, Icarus, 19, 372-389, 1973.

Querry, M. R.: Magnetite, Refractive index database, available at https://refractiveindex.info/?shelf=main&book=Fe3O4& (last access: 02 January 2020), 1985.

Rodríguez-de Marcos, L. V., Larruquert, J. I., Méndez, J. A., Aznárez, J. A.: Quartz, Refractive index database, available at https://refractiveindex.info/?shelf=main&book=SiO2&page=Rodriguez-de_Marcos (last access: 05 January 2023), 2016.

Sinyuk, A., Torres, O., and Dubovik, O.: Combined use of satellite and surface observations to infer the imaginary part of refractive index of Saharan dust, Geophys. Res. Lett., 30, doi: 10.1029/2002GL016189, 2003.

Triaud, A. H. M. J.: Hematite, EODG ARIA, available at http://eodg.atm.ox.ac.uk/ARIA/data?Minerals/Hematite/(Triaud_2005) /hematite_Triaud_2005.ri (last access: 05 January 2023), 2005.